Earth and Space Science

RESEARCH ARTICLE
10.1029/2024EA003887

What Sets the Tropical Cold Point in GSRMs During Boreal Winter? Overshooting Convection Versus Cirrus Lofting

Jacqueline M. Nugent[1,2], **Christopher S. Bretherton**[1,3], **and Peter N. Blossey**[1]

[1]Department of Atmospheric and Climate Science, University of Washington, Seattle, WA, USA, [2]Now at Department of Atmospheric Science, University of Wyoming, Laramie, WY, USA, [3]Allen Institute for Artificial Intelligence, Seattle, WA, USA

Key Points:

- Global storm-resolving models (GSRMs) can reproduce the observed geographic distribution of cold point overshoots
- Radiatively active cirrus near the cold point are underestimated in GSRMs compared to radar/lidar observations
- Cold point-overshooting convection influences the mean cold point but does not entirely explain its variations in temperature or height

Supporting Information:

Supporting Information may be found in the online version of this article.

Correspondence to:

J. M. Nugent,
jnugent2@uwyo.edu

Citation:

Nugent, J. M., Bretherton, C. S., & Blossey, P. N. (2025). What sets the tropical cold point in GSRMs during boreal winter? Overshooting convection versus cirrus lofting. *Earth and Space Science*, *12*, e2024EA003887. https://doi.org/10.1029/2024EA003887

Received 9 AUG 2024
Accepted 10 MAY 2025

Author Contributions:

Conceptualization: Jacqueline M. Nugent, Christopher S. Bretherton
Data curation: Jacqueline M. Nugent
Formal analysis: Jacqueline M. Nugent
Funding acquisition: Christopher S. Bretherton, Peter N. Blossey
Investigation: Jacqueline M. Nugent
Methodology: Jacqueline M. Nugent, Christopher S. Bretherton, Peter N. Blossey
Project administration: Christopher S. Bretherton, Peter N. Blossey
Software: Jacqueline M. Nugent
Supervision: Christopher S. Bretherton
Writing – original draft: Jacqueline M. Nugent

Abstract The cold point tropopause, the minimum temperature within the tropical upper troposphere-lower stratosphere region (UTLS), significantly impacts Earth's climate by influencing the amount of water vapor entering the lower stratosphere. Understanding which mechanisms are most important in setting the cold point temperature and height may help us better predict how it will change in a future warmed climate. In this analysis we evaluate two mechanisms that may influence the cold point—cold point-overshooting convection and the radiative lofting of thin cirrus near the cold point—during boreal winter by comparing 30-day global storm-resolving model (GSRM) simulations from the winter phase of the DYAMOND initiative to satellite observations. GSRMs have explicit deep convection and sufficiently fine grid spacings to simulate convective overshoots and UTLS cirrus, making them promising tools for this purpose. We find that the GSRMs reproduce the observed distribution of cold point-overshooting convection but do not simulate enough cirrus capable of radiative lofting near the cold point. Both the models and observations show a strong relationship between areas of frequent cold point overshoots and colder cold points, suggesting that cold point-overshooting convection has a notable influence on the mean cold point. However, we find little evidence that the radiative lofting of cold point cirrus substantially influences the cold point. Cold point-overshooting convection alone cannot explain all variations in the cold point across different GSRMs or regions; future studies using longer GSRM simulations that consider longer-term UTLS processes are needed to fully understand what sets the cold point.

Plain Language Summary The cold point is the coldest level between the tropical upper troposphere and lower stratosphere. Its temperature determines how much water vapor, a greenhouse gas, can enter the lower stratosphere, and thus can influence how much the Earth warms in the future. The processes that determine the height and temperature of the cold point are not well understood, but two of these may include cooling and moistening by very deep convection that reaches past the cold point itself, called cold point-overshooting convection, and the heating of thin cirrus clouds near the cold point, which causes the surrounding area to gradually lift up. By comparing very high-resolution global climate models that can represent both processes with satellite observations, we find that cold point-overshooting convection has a much stronger influence on the cold point than the lifting from cirrus clouds. However, cold point-overshooting convection does not explain all of the differences between models, suggesting that other processes in this part of the atmosphere, particularly those occurring on time scales longer than the 30-day period of these model simulations, are also important for setting the cold point.

1. Introduction

Water vapor in the lower stratosphere can significantly impact the Earth's climate. Changes in the stratospheric moisture content can increase or decrease the surface warming rate (Solomon et al., 2010). Furthermore, stratospheric water vapor may increase in a warming climate, driving a positive feedback that amplifies surface warming at a rate of 0.3 W m^{-2} K^{-1} (Dessler et al., 2013). The concentration of water vapor in the stratosphere is determined by processes in the upper troposphere-lower stratosphere (UTLS, ∼12–20 km) region. In particular, the tropical cold point tropopause, defined as minimum level in the tropical UTLS temperature profile (Highwood & Hoskins, 1998; Pan et al., 2018; Seidel et al., 2001), acts like a "cold trap" to "freeze-dry" air carried into the lower stratosphere by the Brewer-Dobson circulation (Brewer, 1949; Dessler, 2002; Holton & Gettelman, 2001). Warmer cold point temperatures have been strongly linked to increased moisture in the lower stratosphere, and likewise colder cold point temperatures with a drier lower stratosphere, across many different time scales (Avery

Writing – review & editing: Jacqueline M. Nugent, Christopher S. Bretherton, Peter N. Blossey

et al., 2017; W. J. Randel & Jensen, 2013; W. Randel & Park, 2019; X. L. Zhou et al., 2001b). Changes in the cold point temperature are therefore strongly coupled with changes in the climate.

Deep convection, particularly that which overshoots the cold point tropopause, may play a strong role in determining the cold point temperature and height. The entrainment of overlying stratospheric air by overshooting tops can deepen the convective layer and thereby lower the cold point temperature (Chae et al., 2011; Gettelman et al., 2002; Kuang & Bretherton, 2004; W. Randel & Park, 2019). Proud and Bachmeier (2021) documented an extreme convective event with the coldest cloud top temperatures on record that was associated with an anomalously cold tropopause. Cold anomalies in the cold point temperatures have also been associated with changes in convection from Madden-Julian Oscillation and El Niño-Southern Oscillation cycles (Hatsushika & Yamazaki, 2001; Y.-A. Liou & Ravindra Babu, 2020; X. Zhou & Holton, 2002) as well as the seasonal shift in the Intertropical Convergence Zone (Jain et al., 2011). Suneeth et al. (2017) also found that the cold point became higher and cooler after the respective diurnal peak in convection over both land and ocean regions.

Another possible control on the cold point temperature and height is radiative lofting of cirrus clouds in the Tropical Tropopause Layer (TTL, ∼14–18 km), the transition region between the upper troposphere and lower stratosphere (Fueglistaler et al., 2009). Very thin cirrus near the cold point can have a slight radiative heating effect that can gradually loft the cirrus layer (Ali et al., 2020; Fueglistaler et al., 2009; Jensen et al., 1996). Corti et al. (2006) suggested that this lifting provides a significant fraction of the net mass transport from the TTL to the lower stratosphere.

A more thorough understanding of how overshooting convection influences the cold point temperature may help us understand how the cold point may change in a future warmed climate. Several long-term trends in the cold point have already been identified, including temperature variations linked to an areal expansion of the tropical warm pool (Xie et al., 2015) and a cooling trend over a 25-year period (X.-L. Zhou et al., 2001a) that subsequently shifted to warming (W. Randel & Park, 2019; Yu et al., 2022). Additionally, extreme convective events with very cold cloud top temperatures stemming from anomalously cool cold points may be increasing in frequency (Proud & Bachmeier, 2021). Changes in overshooting convection in a warmed climate may help drive these changes in the cold point temperature. Modeling studies of perturbed climates have found that warmer tropospheric temperatures increase the cold point temperature (Keeble et al., 2021) and that warmer sea surface temperatures lead to more intense convection and more frequent overshoots, especially over oceans (Aumann et al., 2018; Cheng et al., 2022; Wu et al., 2023). It is thus important to understand how cold point-overshooting convection influences the cold point temperature in the current climate so that we can better predict how the cold point temperature, and thus moisture in the lower stratosphere, may change in a future warmed climate.

To determine the relative importance of overshooting convection and cirrus lofting in setting the cold point tropopause, global storm-resolving models (GSRMs) are promising tools. GSRMs have sufficiently fine horizontal grid spacings (<5 km) to explicitly resolve deep convection. By avoiding parameterized deep convection, GSRMs can potentially eliminate many of the biases in simulating convection that global climate models (GCMs) typically have, such as the diurnal cycle of convection over land peaking too early in the day (e.g., Bechtold et al., 2004; Duda & Gallus, 2013). The horizontal grid spacing in GSRMs may be small enough to capture convective overshoots (radii of ∼3 km; Xian & Fu, 2015) that are not resolved by typical GCM grid spacings of around 25–200 km. GSRM vertical grid spacings are typically ∼500 m in the TTL, marginally fine enough to represent cirrus formation processes. Compared to in situ and remote sensing observations which may be coarse or limited in spatiotemporal resolution, GSRMs can provide a complete picture of the atmosphere over space and time and across all parts of the diurnal cycle of convection.

A recent intercomparison of GSRMs from the DYnamics of the Atmospheric general circulation Modeled On Non-hydrostatic Domains (DYAMOND) initiative, detailed in Stevens et al. (2019), provided insight into the range in performance of current GSRMs. Studies analyzing the DYAMOND model output have demonstrated that the DYAMOND GSRMs can reasonably reproduce the overall character of tropical deep convection, radiative effects of cirrus clouds, and zonal-mean water vapor (Dauhut & Hohenegger, 2022; Judt et al., 2021; Nugent et al., 2022; Turbeville et al., 2022) and thus can provide insight into processes in the real atmosphere. These studies also identified significant inter-model differences, particularly in the model microphysics and dynamics, underlining the need for grounding GSRM-based analyses of relationships between tropical convection and cirrus clouds near the cold point with comprehensive observational comparisons.

The goal of this paper is to consider two possible influences on the cold point—overshooting convection and cirrus lofting—and assess which plays a larger role in setting cold point temperature and height in GSRMs using the second (boreal winter) phase of the DYAMOND intercomparison (DYAMOND2; Duras et al., 2021). The rest of this paper is organized as follows. Section 2 describes the DYAMOND2 models, observations, and reanalysis used in this study. Section 3 details the analysis methods for this study, including the definitions of the cold point tropopause and radiatively active cold point cirrus and the general process for adapting the brightness temperature proxy from Nugent and Bretherton (2023). Section 4 describes the background cold point tropopause in the models and observations. In Section 5, we adapt the brightness temperature proxy from Nugent and Bretherton (2023) to the GSRMs and compare the simulated geographic distribution of cold point overshoots to observations. In Section 6, we evaluate the simulated frequency and distribution of the radiatively active cold point cirrus capable of lofting the cold point. Section 7 discusses how these mechanisms, cold point-overshooting convection and radiative cirrus lofting, may contribute to the background cold point temperature in both models and observations. Finally, Section 8 presents a summary and conclusions.

2. Models and Data Sets

2.1. DYAMOND2 Models

The second phase of the DYAMOND initiative, DYAMOND2 (Duras et al., 2021), continues the original DYAMOND initiative described in Stevens et al. (2019) for boreal winter. Twelve GSRMs, all with sub-5 km horizontal grid spacings and explicit (nonparameterized) deep convection, were initialized with the same meteorological analysis and run freely for 40 days from 20 January 2020 to 1 March 2020. This includes a 10-day spinup period, so we only analyze model output from January 30 onward. In addition to the fine horizontal grid spacing, the DYAMOND2 GSRMs have vertical grid spacings of 250–500 m in the UTLS, 15 min 2D output (e.g., surface radiative fluxes and integrated quantities like water vapor path), and 3 hourly 3D output (e.g., vertical profiles of temperature). Most GSRMs use one-moment microphysics schemes while SCREAM uses the two-moment Predicted Particle Properties (P3) scheme (Caldwell et al., 2021; Morrison & Milbrandt, 2015).

In this study, we use five of the DYAMOND2 models: ICON, SCREAM, gSAM, X-SHiELD, and GEOS (see Table 1 for details about the models). These models were chosen because they had full 3D hydrometeor profiles available as of September 2022 when analysis began (SCREAM, X-SHiELD, and GEOS) or were used in our initial study of the DYAMOND1 models in Nugent et al. (2022) and Turbeville et al. (2022) (gSAM and ICON).

We focus on the convectively active tropics during boreal winter and limit analysis to 30°S–10°N. Selecting this range of latitudes rather than the full tropics allows us to focus on locations we expect to experience the most frequent overshooting convection during boreal winter while reducing the data volume needed for analysis. To more easily manage output volume for a detailed analysis of select 3D variables, we use representative 10° × 10° regions described in Section 2.2.

2.2. Analysis Regions

Following Nugent et al. (2022) and Turbeville et al. (2022), we use four representative 10° × 10° latitude-longitude regions to sample land and ocean areas across the tropics for a more thorough analysis of some GSRM outputs. We use two regions that are subsets of the larger study areas used in Nugent and Bretherton (2023): Amazonia (AMZ) and the South Pacific Convergence Zone (SPC). We also study another continental region, South-Central Africa (SCA), and an oceanic region over the Timor Sea (TIM) in the Maritime Continent. These regions and their coordinates are shown in Figure 1. These areas encompass "hot spots" of tropical convection during boreal winter (e.g., Li et al., 2022; Liu & Zipser, 2005; Zipser et al., 2006).

2.3. Observations and Reanalysis

The DYAMOND models are not nudged toward observations or reanalysis during the model run so they do not necessarily reproduce the actual weather systems that occurred during that time period. We instead use observations and reanalysis to evaluate the fidelity of the GSRMs in a statistical sense.

We use ice water content (IWC) from the joint radar/lidar DARDAR-CLOUD v3.10 data set (Delanoë, 2023), which has a horizontal footprint of 1.4 km and 60 m vertical resolution. The DARDAR product merges CloudSat radar and CALIPSO lidar retrievals from the NASA A-Train, which crosses the equator daily at 01:30 and 13:30

Table 1
List of DYAMOND2 Models

Abbreviation	Model name	Reference(s)	Horiz. grid spacing (km)	Vertical levels	Model top
ICON	Icosahedral Non-hydrostatic Model	Zängl et al. (2015), Klocke et al. (2017)	2.5	90	75 km
gSAM	Global System for Atmospheric Modeling	Khairoutdinov et al. (2022)	4.3	74	37 km
GEOS	Goddard Earth Observing System	Putman and Lin (2007), Putman and Suarez (2011), Putman (2021)	3.25	181	80 km
SCREAM	Simple Cloud-Resolving E3SM Atmospheric Model	Caldwell et al. (2021)	3.25	128	40 km
X-SHiELD	eXperimental System for High-resolution prediction on Earth-to-Local Domains	Lin (2004), Harris et al. (2020, 2023)	3.25	79	3 hPa

Note. DYAMOND2 models used in this study.

local time. The DARDAR-detected "ice" inherently includes all frozen hydrometeors while all models except SCREAM distinguish between cloud ice, snow, and graupel; we use "frozen water" when referring to the sum of all frozen hydrometeors in the GSRM output to avoid confusion. We convert the DARDAR IWC to a mixing ratio using reference densities from a standard tropical atmosphere profile. For brightness temperature data, we use infrared brightness temperatures derived from geostationary satellites in the NCEP/CPC L3 Half Hourly 4 km Global (60°S–60°N) Merged IR V1 (GPM_MERGIR) data set (Janowiak et al., 2017). This data set has a 4 km horizontal resolution, comparable to the DYAMOND GSRMs, and a temporal resolution of 30 min.

We compare the GSRM temperature output to hourly temperature profiles from the ECMWF Reanalysis v5 (ERA5) reanalysis (Hersbach et al., 2020). The ERA5 data is mapped to a 0.25° × 0.25° grid and has 137 vertical levels, corresponding to a vertical resolution of 300–400 m in the UTLS (Hersbach et al., 2017). Using the ERA5 reanalysis as an observational comparison allows us to more directly compare these model results to the climatology from Nugent and Bretherton (2023). To supplement the model-observations comparison for temperature, we also examine radiosonde data from the Integrated Global Radiosonde Archive (IGRA) for several stations located within or just outside of the analysis regions. We use a total of eight stations: five in TIM (station IDs 97372, 97724, 94120, 97900, 97180), one in SCA (67774), one in the SPC (91643), and one in AMZ (87155). The mean cold point temperature and height across all stations within each region is compared with the GSRMs and reanalysis.

To maximize the sample size available for observational comparisons, we primarily use DARDAR, ERA5, and GPM_MERGIR data from December-January-February (DJF) 2007–2010. Since CloudSat only operated during the daytime after 2010, 2007–2010 is the only time period available in the DARDAR-CLOUD data set that offers combined radar-lidar retrievals during day and night for DJF. This time period also aligns with the climatology in Nugent and Bretherton (2023). Over the boreal winter periods of 2007–2010, the average Quasi-Biennial Oscillation (QBO) index is similar to the QBO index during boreal winter 2020 (Figure S1 in Supporting Information S1). The 2007–2010 period also experienced a mix of El Niño and La Niña phases compared to a weak

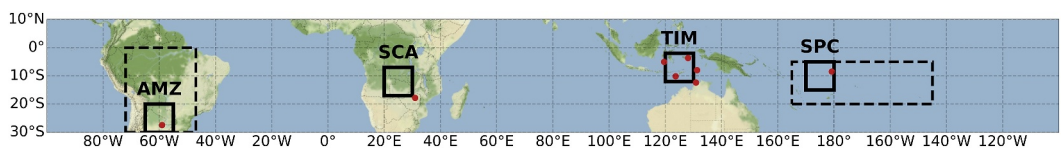

Figure 1. Map of the 10 ° × 10° analysis regions within the tropics. From left to right: Amazonia (AMZ; 65°W–55°W, 30°S–20°S), South-Central Africa (SCA; 20°E–30°E, 17°S–7°S), Timor Sea (TIM; 120°E–130°E, 12°S–2°S), and the South Pacific Convergence Zone (SPC; 170°–180°E, 15°S–5°S). Red dots show the station locations of the IGRA soundings used. The dashed boxes depict the larger AMZ and SPC regions used in Nugent and Bretherton (2023).

El Niño that occurred during 2020 (Figure S1 in Supporting Information S1). Overall, we thus expect atmospheric conditions most relevant to the UTLS to be similar between the two time periods. For the frequency maps of cold point overshoots in Section 5.2, we use reanalysis from February 2020 for a more direct comparison with the DYAMOND2 output. Except for the radiosonde station in the SCA region, all sounding profiles are from February 2020. The SCA station (67774) record ended in 2017, so we use February 2002 instead which had similar climatological conditions to 2020. For most analyses, we resample the ERA5 data to match the 3D temporal output frequency (3 hourly) of the DYAMOND2 GSRMs.

3. Analysis Methods

3.1. Cold Point Tropopause

We define the cold point tropopause using the level of the minimum temperature on a $0.25° \times 0.25°$ grid as in Nugent and Bretherton (2023). To match the DYAMOND models to the reanalysis, we first take the mean temperature profile over a $0.25° \times 0.25°$ area and then calculate the cold point from the coarsened grid. The uncertainties in the ERA5 reanalysis temperatures are described more thoroughly in Nugent and Bretherton (2023), but we expect an uncertainty around ±120–200 m (Hoffmann & Spang, 2022) in the tropopause height and a slight warm bias of <0.5 K in the cold point temperature (Tegtmeier, Anstey, Davis, Dragani, et al., 2020). This definition is applied to ERA5 reanalysis and the GSRMs in Section 4.

3.2. Brightness Temperature Proxy for Cold Point Overshoots

To identify cold point-overshooting convection in the GSRMs, we adapt the brightness temperature proxy developed in Nugent and Bretherton (2023). Since brightness temperature was not a saved output in any of the models, we estimate the broadband brightness temperature (T_b) from model output of outgoing longwave radiation (OLR) using the inverse Planck function: $OLR = \sigma T_b^4$. The resultant broadband brightness temperature is not the same as the GPM_MERGIR IR brightness temperatures used in Nugent and Bretherton (2023) and the observational comparisons here, but we expect it to be close in cloudy regions of low OLR/low T_b. We calibrate the proxy as in Nugent and Bretherton (2023) by binning frozen water mixing ratios by $T_b - T_{cp}$, where T_{cp} is the cold point temperature, at levels relative to the local 0.25° cold point height (z_{cp}) in the GSRMs. This binning process combines methods similar to Dauhut and Hohenegger (2022) and Pan and Munchak (2011). Recalibrating the observed proxy from Nugent and Bretherton (2023) for the GSRMs ensures that any differences between the estimated and actual T_b in the models are accounted for. As ICON and gSAM did not save the full 3D profiles of snow or graupel, we cannot calculate the total frozen water mixing ratio that would be equivalent to the DARDAR-observed ice, so we omit these two models from our calibration process. The identified cold point overshoots in ICON and gSAM therefore may not be perfectly representative of the actual simulated overshoots. For the observations, we use the DJF 2007–2010 observational data from the larger SPC and AMZ regions used in Nugent and Bretherton (2023), because the limited sampling from the DARDAR instrument means that the $10° \times 10°$ regions do not have sufficient sample size to capture the actual relationship between frozen water and $T_b - T_{cp}$, even over this time period. Results from this calibration process for the observations and the GSRMs are shown in Section 5.1.

3.3. Radiatively Active Cold Point Cirrus

To evaluate the potential for radiative lofting of cirrus near the cold point in the GSRMs, we must identify cirrus in the DYAMOND2 output that can produce a radiative heating rate strong enough to lead to net upward motion. However, vertical profiles of heating rates or optical depth were not commonly saved model output for the DYAMOND2 GSRMs. We therefore identify "radiatively active cold point cirrus" (hereafter "RACP cirrus") using the ice mixing ratio alone by finding the approximate cloud ice concentration needed for a cirrus cloud near the cold point whose radiative heating rate can induce ascent sufficient to offset its ice fall velocity. An ice crystal with a radius of 10.6 μm, typical of cirrus near the cold point (Krämer et al., 2016), would have a fall velocity of $w_t = 20$ mm/s (Dinh et al., 2010). Assuming an environmental potential temperature stratification of $\frac{d\theta}{dz} = 3.5$ K/km, a radiative heating rate exceeding $w_t \frac{d\theta}{dz} = 6$ K/day is needed to force net upward motion of the falling ice.

To calculate the critical ice concentration, we consider an idealized cirrus cloud near the cold point at 17 km altitude with a temperature of $T_i = 195$ K and a geometric thickness of $\Delta z = 1$ km. We assume the incident

broadband longwave radiation at the bottom of the cloud is $F_i = 260$ W/m^2, typical of a clear sky region in the tropics. The net upwelling longwave radiation absorbed by a cloud of optical depth τ is given by

$$F_{abs} = \left(F_i - 2\sigma T_i^4\right)\left(1 - e^{-\tau}\right) \quad (1)$$

where σ is the Stephan-Boltzmann constant. This induces a heating rate $\partial T/\partial t = F_{abs}/(\rho c_p \Delta z)$, where c_p is the specific heat of air at constant pressure and $\rho \approx 0.15$ kg/m^3 is the air density at 17 km in a standard tropical atmosphere. Solving for τ reveals that to achieve a heating rate of $\partial T/\partial t = 6$ K/day, the idealized cloud would need an optical depth of 0.1.

We estimate the cloud ice mixing ratio q_i needed for this 1 km cloud to reach an optical depth of 0.1 using Equation 7.3.15c in K.-N. Liou (2002):

$$\tau \approx \text{IWC}\ \Delta z\left(c + \frac{b}{D_e}\right) \quad (2)$$

where IWC is the ice water content $\left(\rho * q_i\right)$, D_e is the effective diameter, and b and c are constants ($b \approx 3.686$ m$^2\mu$m g^{-1}, $c \approx -6.656 \times 10^{-3}$ m^{2}g^{-1}). With $D_e = 21.2$ μm (i.e., twice the ice crystal radius), Equation 2 yields a cloud ice mixing ratio of 4×10^{-6} kg/kg. Small changes in the assumed values do not substantially change this result.

Therefore, we define RACP cirrus in the GSRMs as columns near the cold point with a cloud ice concentration of $>4 \times 10^{-6}$ kg/kg. This definition is applied to the observations and GSRMs in Section 6.2.

4. Cold Point Tropopause in Observations and GSRMs

Figure 2 shows the time- and area-mean UTLS temperature profiles of the four analysis regions for the DYAMOND models and ERA5 reanalysis. The mean cold point temperature and height from available radiosonde data (black crosses; see Figure 1 for station locations) is also included for further comparison. Note that IGRA data is available from five locations in and around the TIM region, but only one location in each of the other regions; the small sample size of radiosonde profiles in SPC, AMZ, and SCA means that the mean cold points from the radiosondes may not be entirely representative of the region as a whole.

The GSRM temperature profiles generally scatter around the ERA5 profiles. The simulated cold points have heights around 16.5 to 17.5 km and temperatures from 186 to 192 K over oceans and 190 to 197 K over land, generally within 5 K and 0.5 km of the reanalysis. However, the radiosonde cold points are cooler than most of the GSRMs in the SPC and TIM and are higher than the cold points in SCA for all but X-SHiELD. gSAM consistently has the lowest and coldest mean cold points of all the GSRMs, while X-SHiELD is generally the highest; the other GSRMs do not have clear trends between regions. Both the GSRMs and the reanalysis have good agreement with the mean IGRA radiosonde cold points in AMZ (Figure 2b).

In Figure 3 we compare both the temperature and height of the cold point across the tropics over the 30-day period between ERA5 and the GSRMs. The mean cold point temperatures are remarkably similar between the models and the observations. All GSRMs simulate the coldest cold points over the Pacific warm pool, consistent with the observations. Cold points over the oceans tend to be slightly colder in the GSRMs, although this may be partially due to the slight warm bias (<0.5 K) in the ERA5 climatological cold point (see Section 2.3). There is more variation in the cold point heights between the models, but the heights within each model are more consistent geographically than the temperatures. X-SHiELD (Figure 3k) has the highest cold points while ICON, GEOS, and SCREAM are in good agreement with the ERA5 cold point heights. As in Figure 2, while gSAM (Figures 3g and 3h) simulates the lowest and the coldest cold points of the DYAMOND2 GSRMs, its cold point pressure is not the largest among the models (not shown). Unlike the other DYAMOND2 models shown here, gSAM is an anelastic model (Khairoutdinov et al., 2022) and the additional approximations in the model equations cause the UTLS temperature profile in height space to look different from the other models.

In ERA5 and the GSRMs, there is a strong positive association between higher cold point heights (>18 km) and warmer cold point temperatures (>200 K) from 20°S–30°S between ~120°W and 100°W (lower right corner of

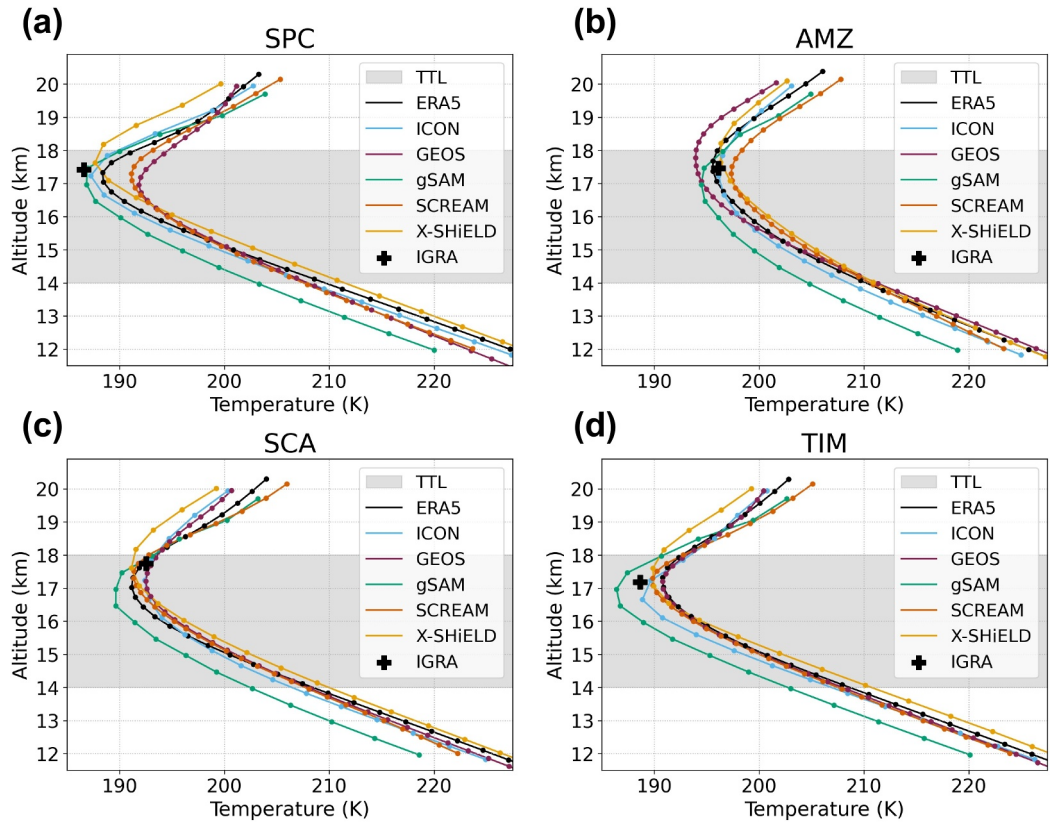

Figure 2. Time- and area-mean temperature profiles for the DYAMOND2 GSRMs and ERA5 reanalysis in the (a) SPC, (b) AMZ, (c) SCA, and (d) TIM regions. The TTL is shaded in gray. Crosses mark the mean cold point height and temperature from IGRA soundings in each region.

each panel in Figure 3). This feature is surprising given that warmer temperatures generally correspond to lower heights in the troposphere. One possible explanation is that the models are simulating double tropopause events, which primarily happen in the midlatitudes (W. J. Randel et al., 2007), as they shift from tropical to extratropical temperature profiles between 20°S and 30°S. Our method for identifying the cold point tropopause simply takes the level of the minimum UTLS temperature, which in some cases may identify the higher (secondary) tropopause as the cold point if it is marginally colder than the primary tropopause.

Overall, the GSRMs reasonably reproduce the observed cold point temperatures and heights, but with some key inter-model differences across regions. These differences underscore the importance of using cold point-relative metrics to identify cold point cirrus and overshoots rather than fixed altitude levels.

5. Cold Point-Overshooting Convection

5.1. Calibrated Brightness Temperature Proxy in the GSRMs

We calibrate the brightness temperature proxy introduced in Nugent and Bretherton (2023) as described in Section 3.2 for the DYAMOND2 GSRMs and coinciding DARDAR data. The bin-mean cloud-conditional frozen water and $T_b - T_{cp}$ bin counts for DARDAR observations, X-SHiELD, GEOS, and SCREAM are shown in Figure 4 for the SPC (see Figure S2 in Supporting Information S1 for the AMZ). The bottom row below the thick black line in Figure 4 and Figure S2 in Supporting Information S1 gives the total number of occurrences of each $T_b - T_{cp}$ bin (i.e., regardless of whether ice or frozen water was detected). There are substantial inter-model differences in the cold point-relative frozen water mixing ratios. At brightness temperatures warmer than the cold point (to the right of the dashed lines in Figure 4), the models simulate vastly different amounts of frozen water from each other and from the observations. SCREAM has very little frozen water outside of the areas of deep convection with low T_b, both in terms of amount and frequency, while X-SHiELD has too much of both.

10.1029/2024EA003887

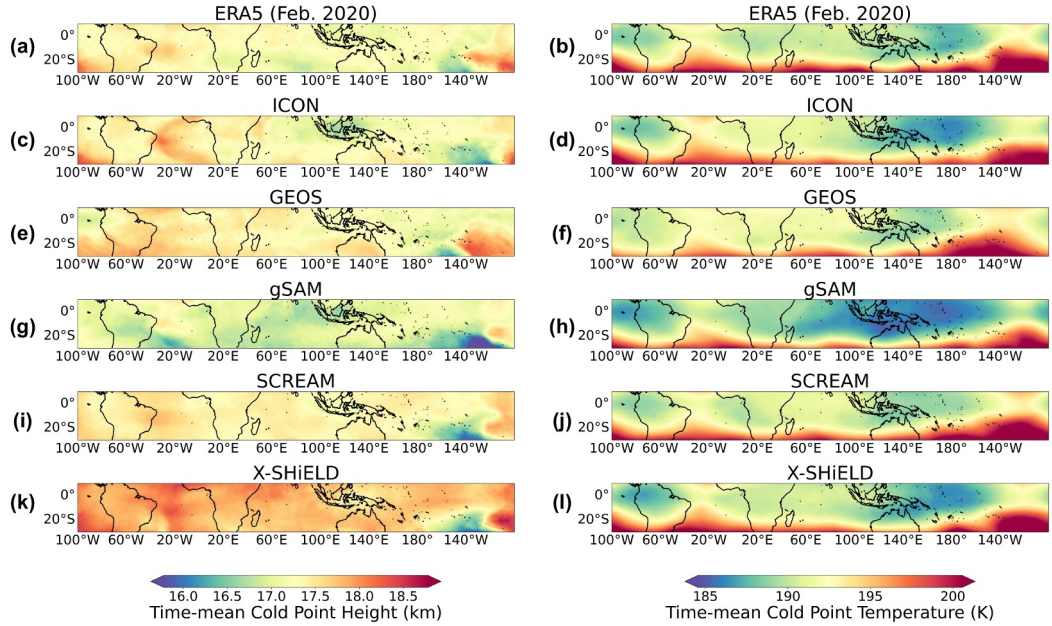

Figure 3. Time-mean 0.25° cold point height (left) and temperature (right) for (a)–(b) ERA5, (c)–(d) ICON, (e)–(f) GEOS, (g)–(h) gSAM, (i)–(j) SCREAM, and (k)–(l) X-SHiELD. The color map is centered on the tropics-mean ERA5 cold point values such that blue-green (orange-red) colors indicate areas of lower/colder (higher/warmer) cold points.

GEOS has more frozen water than the observations at z_{cp} and z_{cp} + 500 m, but not as much as in X-SHiELD. In both GEOS and SCREAM, there is much less frozen water near the cold point at higher T_b than in the observations, suggesting that thin cirrus located above the cold point are underrepresented in these GSRMs. There is little regional variation in the binned frozen water between the SPC (Figure 4) and AMZ (Figure S2 in Supporting Information S1). The inter-model differences far exceed the regional differences, as Nugent et al. (2022) and Turbeville et al. (2022) found for the DYAMOND1 models.

In Figure 5, we restrict the DARDAR observations to pixels where both the CloudSat radar and CALIPSO lidar detect ice as in Nugent and Bretherton (2023). Since we cannot restrict the GSRM output by instrument type, we instead set a minimum frozen water mixing ratio threshold of 2.5×10^{-4} kg/kg. In the observations, this mixing ratio threshold results in an ice distribution that is very similar to the radar-lidar distribution, so we expect it to be a good approximation for what would be detectable by both radar and lidar in the GSRMs. These restrictions should exclude thin cirrus that could not be detected by the radar and thus limit the analysis to cirrus likely related to convection and cold point-overshooting tops. SCREAM, and to a lesser extent GEOS, indeed have much less frozen water above the cold point at higher T_b. However, from Figures 4 and 5 the bin counts decrease almost uniformly across T_b bins in X-SHiELD, which further suggests that thick cirrus with anomalously high frozen water content exist above the cold point at high T_b in X-SHiELD. As with Figure 4, there are few regional differences between models in the binned plots (see Figure S3 in Supporting Information S1 for the AMZ).

As in Nugent and Bretherton (2023), we calculate the fraction of convective cirrus and "other stratospheric cirrus" that lie above the cold point. In the DARDAR observations, we calculate the fraction of retrievals with ice detectable by both the radar and lidar for convective cirrus fraction and lidar-only retrievals for other stratospheric cirrus. In the GSRMs, we use the fraction of columns with frozen water mixing ratios $\geq 2.5 \times 10^{-4}$ kg/kg to find the convective cirrus fraction and the fraction of columns with frozen water mixing ratios between 1×10^{-6} kg/kg and 2.5×10^{-4} kg/kg for other stratospheric cirrus. GSRMs simulate about 5 times less other stratospheric cirrus in the AMZ (a land region) than in the observations (~0.5% vs. 2.6%), but more convective cirrus (0.02%–0.03% vs. 0.01%). The intermodel spread in other cirrus is much larger in the SPC (an ocean region), ranging from 0.08% in GEOS to 1.4% in X-SHiELD versus 2.4% in the observations. While the other stratospheric cirrus fraction in the SPC is closest to the observations in X-SHiELD, the convective cirrus fraction is larger (0.06% vs. 0.04%). Overall, thin cirrus above the cold point are underrepresented in the GSRMs except for X-SHiELD, which simulates too much frozen water everywhere near the cold point.

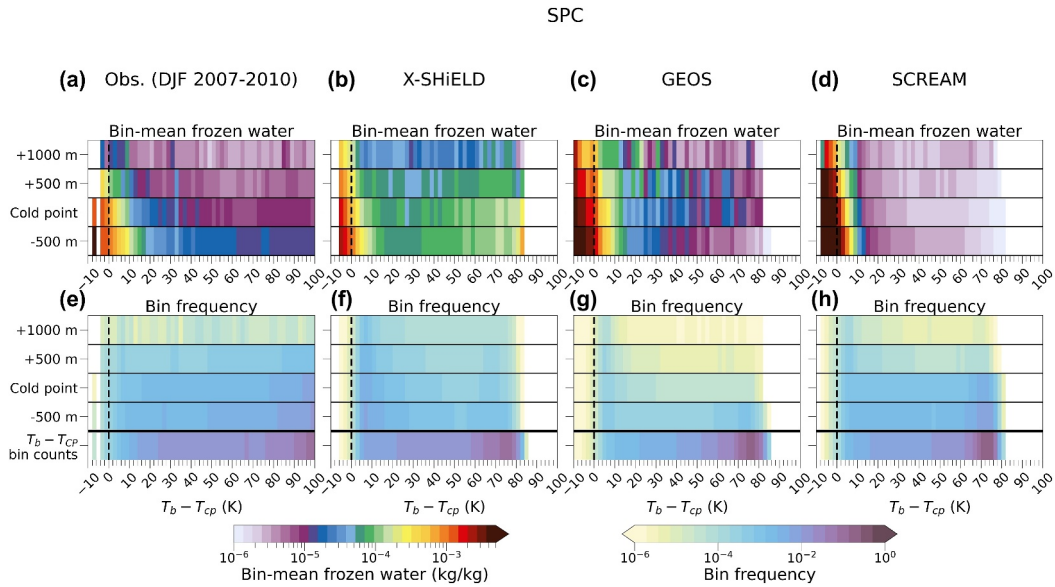

Figure 4. Cold point-relative frozen water binned by $T_b - T_{cp}$ in the SPC region for (a) DARDAR observations, (b) X-SHiELD, (c) GEOS, and (d) SCREAM. The top row of plots shows the bin-mean cloud-conditional frozen water mixing ratio at 500 m below to 1,000 m above the local cold point height. The bottom row of plots shows the bin counts conditioned on when (e) DARDAR detects ice or (f)–(h) the GSRM frozen water exceeds a lower threshold of 1×10^{-6} kg/kg. The total $T_b - T_{cp}$ bin counts are shown below the thick black line in the bottom row of plots. The dashed lines mark where the brightness temperature equals the cold point temperature. The bin width is 2 K.

Joint histograms of T_b and T_{cp} are shown in Figure 6 for the SPC and Figure 7 for the AMZ (see Figures S4 and S5 in Supporting Information S1 for TIM and SCA, respectively). For the observations, the ERA5 and GPM_MERGIR data is not restricted to the times and locations of DARDAR retrievals and thus are directly comparable to the GSRM histograms. In clear sky regions, however, the observations will have higher T_b because of the simplified T_b calculation we use for the GSRMs. In the observations and GSRMs, the frequency of values with $T_b < T_{cp}$ (below the solid line in Figures 6 and 7), corresponding to cold point-overshooting convection, is similar between the $10^\circ \times 10^\circ$ ocean and land regions. However, the general shape of the distributions differs between regions. The distribution of T_{cp} is wider in the AMZ than in the SPC (Figure 6) or TIM regions (Figure S4 in Supporting Information S1), meaning there is a larger range in cold point temperatures over the Amazon than over the ocean. The SCA land region, however, more closely resembles the oceanic distribution of cold point temperatures (Figure S5 in Supporting Information S1). The distribution in the AMZ bulges slightly along the $T_b = T_{cp}$ line toward low T_b and low T_{cp} (175–200 K and 180–185 K, respectively, in Figure 7a). This small "tail" corresponds to the more frequent deep convection in the AMZ that does not reach the cold point. This tail is not apparent in the observations in the SPC or TIM histograms (Figure 6a and Figure S4a in Supporting Information S1), consistent with the generally less intense deep convection observed over oceans than land regions (e.g., Liu & Zipser, 2005; Zipser et al., 2006).

These observed regional patterns are largely reproduced by the GSRMs. However, gSAM, SCREAM, and X-SHiELD simulate a low T_b/low T_{cp} tail in the TIM region (Figures S4d–S4f in Supporting Information S1), suggesting that these models produce more frequent deep but not cold point-overshooting convection than the others over the Maritime Continent. Another exception is GEOS (Figure 6c), which does not have the low T_b/low T_{cp} tail in the SPC. Instead, GEOS has a tail on the opposite side with low T_b but high T_{cp} (~197–200 K; Figure 6c).

Overall, we conclude that $T_b < T_{cp}$ is an effective proxy for identifying likely cold point overshoots in the GSRMs (GEOS, SCREAM, and X-SHiELD) as well as in the observations.

5.2. Geographic Distribution of Cold Point Overshoots

The 3 hourly temporal resolution and 30-day period of the DYAMOND models results in a much smaller sample size than the ERA5/GPM_MERGIR climatology from Nugent and Bretherton (2023). Therefore, in Figure 8 we

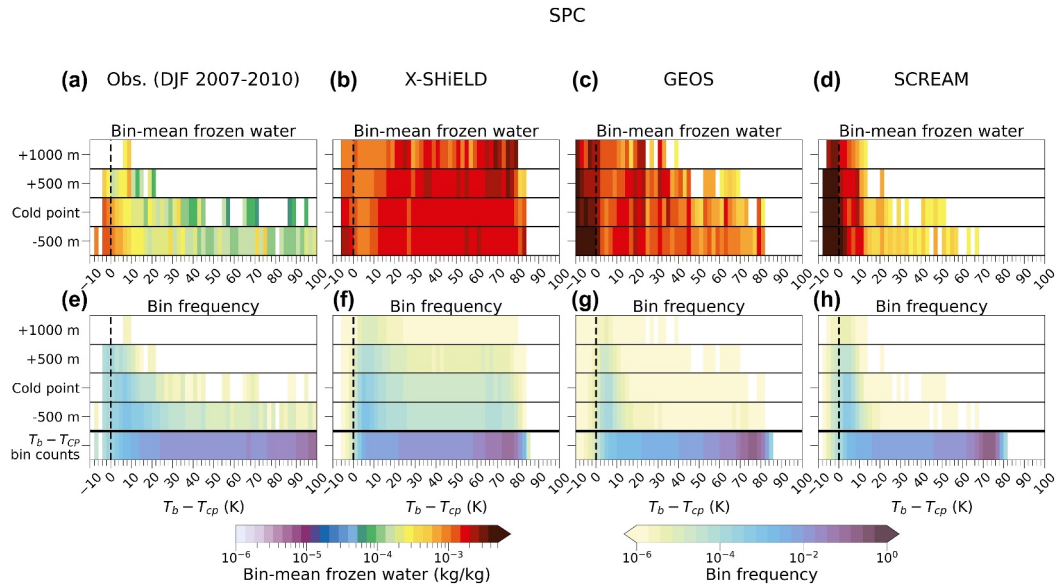

Figure 5. As in Figure 4, but restricted to (a, e) DARDAR pixels detected by both the radar and lidar or (b, f)–(d, h) GSRM grid points where the mixing ratio at that level exceeds 2.5 × 10^{-4} kg/kg.

evaluate the frequency of cold point overshoots within 5° × 5° boxes across the tropics. Each 5° × 5° box contains 13,000 to 48,000 grid cells depending on the model grid spacing. We calculate the 5° × 5° frequencies by summing the number of instances of cold point overshoots within each box and dividing by the total number of

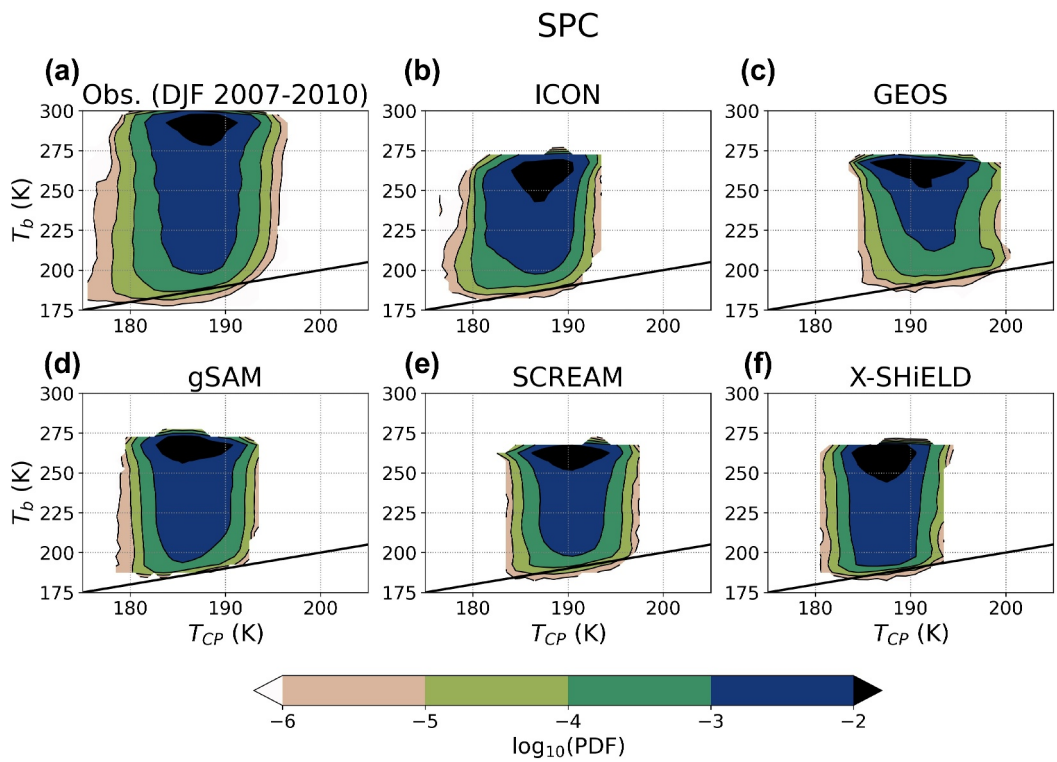

Figure 6. Joint brightness temperature-cold point histograms for all data points in the SPC region in (a) ERA5/GPM_MERGIR observations, (b) ICON, (c) GEOS, (d) gSAM, (e) SCREAM, and (f) X-SHiELD. The solid lines mark where the brightness temperature equals the cold point.

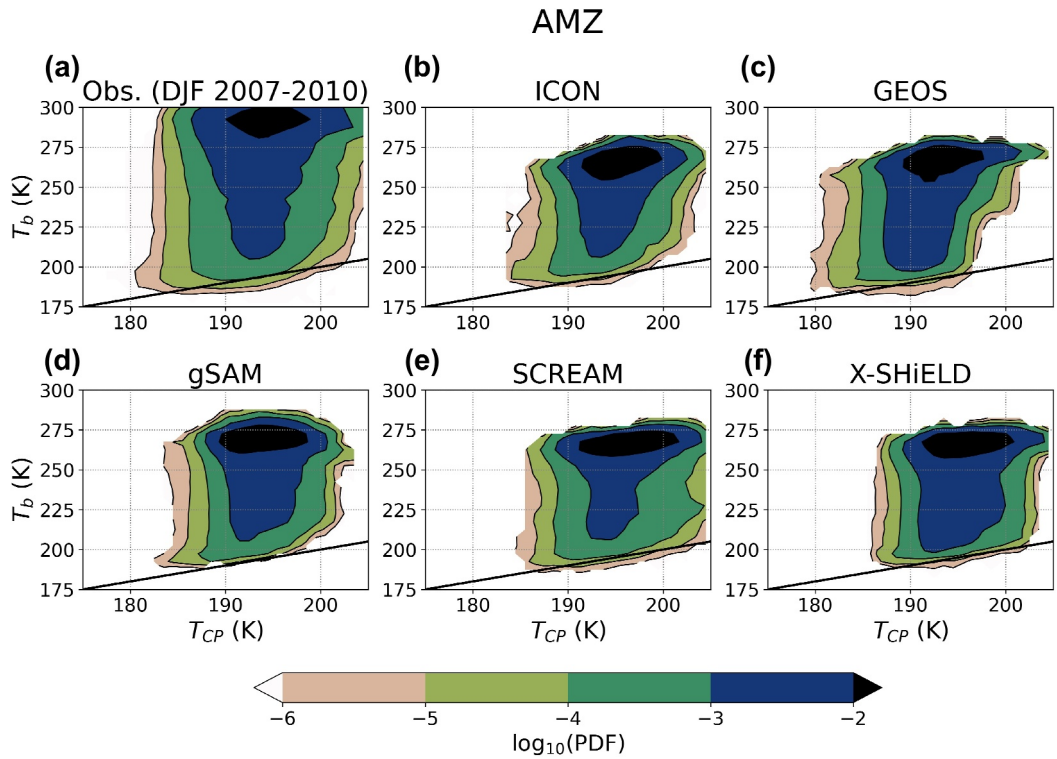

Figure 7. As in Figure 6, but for the AMZ region.

profiles (i.e., the number of grid cells times the number of time steps). To match the DYAMOND output for a fair comparison, we use ERA5 cold point and GPM_MERGIR brightness temperature data from February 2020 sampled every 3 hr.

Except for gSAM, the spatial distribution of cold point overshoots shown in Figure 8 is strikingly similar between the GSRMs and the observations. Therefore, despite the inter-model differences in cold point temperatures (Figures 2 and 3) and deep convection (Figures 4 and 5), the models simulate cold point overshoots in a very similar manner. However, the slight favoring of land regions over ocean regions in observed cold point overshoots is not reproduced by all of the GSRMs. SCREAM, and to a lesser extent X-SHiELD, tends to simulate cold point overshoots too often over oceans relative to the amount it simulates over land regions. Deep convection, especially updraft speeds, may therefore be too vigorous over the oceans in SCREAM and X-SHiELD, allowing convection to penetrate the cold point too frequently.

The observations reveal the hot spots in overshooting convection over Africa, South America, the Maritime Continent, and the Pacific warm pool expected from previous studies (e.g., Li et al., 2022; Liu & Zipser, 2005; Takahashi & Luo, 2014; Zipser et al., 2006). Cold point overshoots favor the land areas overall, consistent with the climatology from Nugent and Bretherton (2023), although many of the boxes with ≥10% frequency occur over ocean areas. ICON and GEOS reproduce this pattern well with the expected hot spots, especially over the Maritime Continent. SCREAM also simulates more overshoots over oceans than land, but cold point overshoots occur less often than in the other models, even in the highest frequency boxes. The lower frequency could be caused by the "popcorn"-like texture of simulated convection in SCREAM (Caldwell et al., 2021) since the simulated overshoots may not cover as much area as in the other GSRMs. X-SHiELD simulates nearly equal amounts of cold point overshoots over land and oceans, consistent with findings from Harris et al. (2023) who used a similar configuration of X-SHiELD.

The apparent lack of cold point overshoots in gSAM in Figure 8d is more likely due to the $T_b < T_{cp}$ proxy than the performance of gSAM itself. Because cloud ice is the only radiatively active frozen hydrometeor in gSAM, the brightness temperature estimated from OLR may not reflect the vertical structure of deep convection. This difference would make it more difficult for clouds to have $T_b < T_{cp}$ (note the lack of grid points with $T_b < T_{cp}$ in

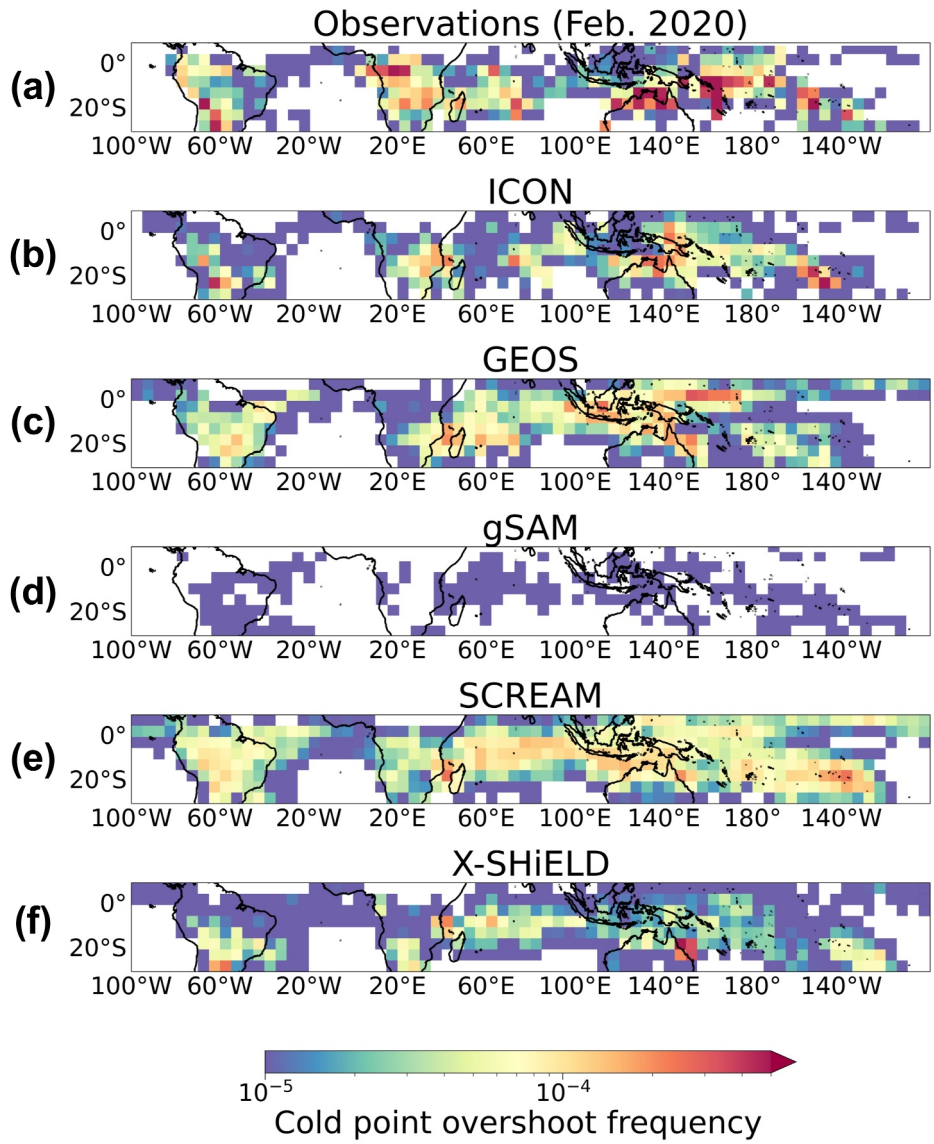

Figure 8. Frequency of cold point overshoots in the 30-day period within 5 ° × 5° latitude-longitude boxes for (a) ERA5/GPM_MERGIR observations and (b) ICON, (c) GEOS, (d) gSAM, (e) SCREAM, and (f) X-SHiELD GSRMs. The observations have been sampled every 3 hr to match the temporal resolution of the DYAMOND GSRMs. The apparent lack of cold point overshoots in gSAM should be disregarded; see the text for details.

Figures 6 and 7d) and could allow significant amounts of ice above the cold point when $T_b > T_{cp}$. However, we cannot properly adjust the brightness temperature proxy for gSAM without the full 3D profiles of snow or graupel. The apparent underestimation of cold point overshoots in gSAM in Figure 8d should therefore be disregarded; more work is needed to determine how often cold point overshoots actually occur in gSAM.

In the GSRMs and observations, cold point overshoots seem to be related to the mean cold point temperature. Within each model, areas with the highest frequency of cold point overshoots in Figure 8 tend to be collocated with areas of the coldest cold points (right column of plots in Figure 3) in that model, particularly in the Indo-Pacific warm pool. One exception is in the region of relatively warm and low cold points near 140°W, ∼30°S–20°S (Figure 3) in all of the GSRMs and ERA5, but this overshoot region lies outside the deep tropics (15°S–15°N) and is subject to different large-scale dynamical controls on tropopause height. These patterns suggest that overshoots may decrease cold point temperature, influencing the spatial variability of the mean cold point across the deep tropics.

Overall, the GSRMs credibly reproduce the observed frequency and spatial distribution of cold point-overshooting convection.

6. Radiative Lofting of Cold Point Cirrus

6.1. Frequency of Radiatively Active Cold Point Cirrus

We identify the frequency of RACP cirrus in the GSRMs and observations using the threshold defined in Section 3.3. Figure 9 shows histograms of cold point-relative cloud ice $>4 \times 10^{-6}$ kg/kg for the GSRMs in the SPC. For the observational comparison, we use DARDAR data from February 2007 to 2010. On average, each $5^\circ \times 5^\circ$ box includes a total of ∼19,000 DARDAR retrievals across the entire time period, comparable to the number of grid points for the GSRMs during February 2020. Here, we plot the cloud ice distributions at the z_{cp}-relative levels used in Figures 4 and 5 as well as $z_{cp} - 1000$ m to get an idea of how the RACP cirrus frequency changes with height around the cold point. The bold green lines in Figure 9 indicate the frequency of RACP cirrus at z_{cp}; the model-observation differences at this level are particularly important for evaluating the radiative lofting of cirrus through the cold point in the GSRMs. Since the P3 microphysics scheme in SCREAM does not partition frozen hydrometeors into separate categories, the histogram in Figure 9e is actually for frozen water rather than cloud ice alone as it is in the other models. However, because cold point-overshooting tops are rare compared to RACP cirrus near the cold point, we do not expect the larger-sized ice categories to significantly affect the overall distribution.

In the models and the observations, there is a consistent decrease in cloud ice with height, with a strong drop-off above the cold point. However, the amounts of cirrus at each level vary greatly between models and observations (Figure 9). RACP cirrus are greatly underestimated in the GSRMs at all levels, except for X-SHiELD at $z_{cp} + 1000$ m in the SPC. Otherwise, the RACP cirrus fractions in the GSRMs (numbers on each panel of Figure 9) are typically ∼2–30 times less than in the observations at each level. X-SHiELD is the closest to the DARDAR observations, but still underestimates the frequency of RACP cirrus by a factor of ∼2–5. All GSRMs are particularly deficient in RACP cirrus at z_{cp}.

Over land in the AMZ (Figure 10), the cirrus frequencies in the models and observations still consistently decrease from $z_{cp} - 1000$ m to $z_{cp} + 1000$ m, but are generally less than half as much as over the ocean in the SPC (Figure 9). GEOS (Figure 10c) is the exception, with cirrus fractions 3–4 times greater over land at all levels. In the observations in the AMZ (Figure 10a), there are secondary peaks in the histogram around 2×10^{-5} kg/kg at $z_{cp} - 1000$ m and $z_{cp} - 500$ m and around 7×10^{-5} kg/kg at z_{cp}. These secondary peaks are not present in any of the GSRM distributions. However, in all but gSAM, the frequency distributions become flatter at higher ice water mixing ratios. The secondary peaks in the observed distribution and the ice at 1×10^{-5} kg/kg to $\sim 5 \times 10^{-4}$ kg/kg in the models are likely due to deep convection that reaches up to the cold point or thicker convectively detrained anvils. In the GSRMs, deep convection may be deeper than in the observations and penetrate further past the cold point, resulting in higher ice concentrations near the cold point. As in the SPC, the overall frequencies of RACP cirrus in the AMZ, especially at z_{cp}, is much less in the GSRMs than in the observations (Figure 10).

We expect these results to be robust to the choice of parameters used to set the RACP cirrus threshold in Section 3.3. Changes in the assumptions that led to the 4×10^{-6} kg/kg threshold, such as the environmental lapse rate, would change the minimum cloud ice concentration needed for the idealized cirrus cloud to loft. However, adjusting the threshold in either direction to make more or less RACP cirrus still would not make up for the substantial differences between the GSRMs and observations.

6.2. Distribution of Radiatively Active Cold Point Cirrus

In Figure 11, we replicate the map of $5^\circ \times 5^\circ$ cold point overshoot frequencies in Figure 8 for RACP cirrus frequencies at z_{cp} (i.e., $q_i > 4 \times 10^{-6}$ kg/kg; see Section 3.3). As explained in Section 3.3, these cirrus should be capable of lofting above the cold point if the underlying column is cloud-free. The RACP cirrus located at the cold point level are of particular interest because they have the greatest potential to loft the cold point in the following time step. We again calculate the frequencies in each $5^\circ \times 5^\circ$ box by dividing the total number of instances of RACP cirrus at z_{cp} by the total number of columns in space and time. As in Figures 9 and 10, we compare the

10.1029/2024EA003887

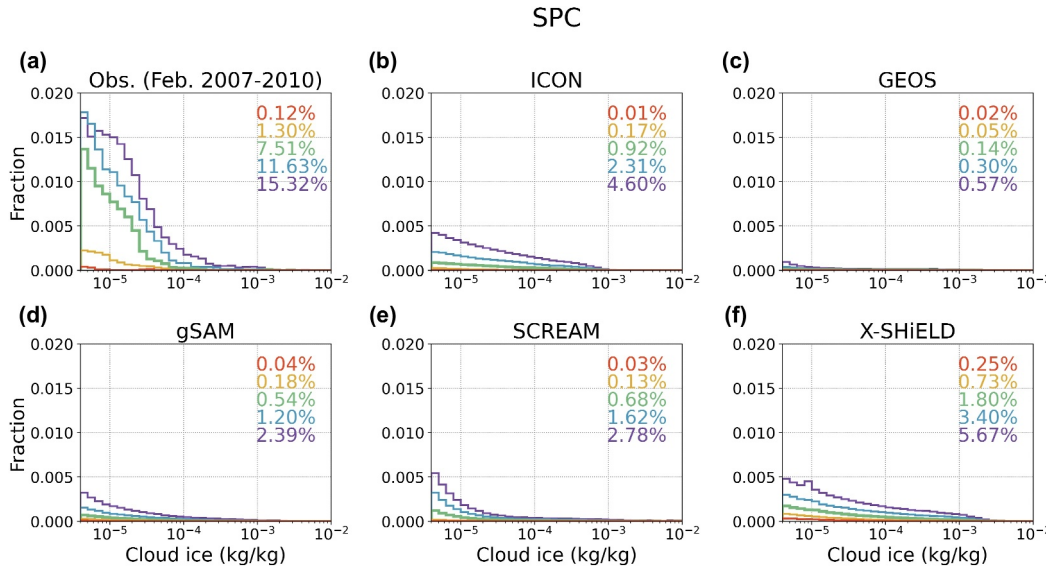

Figure 9. Histograms of cloud ice above the radiatively active threshold (4×10^{-6} kg/kg) at levels relative to the cold point for (a) DARDAR observations and (b) ICON, (c) GEOS, (d) gSAM, (e) SCREAM, and (f) X-SHiELD GSRMs in the $10^{\circ} \times 10^{\circ}$ SPC region. The numbers in the figure give the cloud fraction of radiatively active cirrus at each z_{cp}-relative level: $z_{cp} - 1000$ m (purple), $z_{cp} - 500$ m (blue), z_{cp} (green), $z_{cp} + 500$ m (yellow), and $z_{cp} + 1000$ m (red).

GSRMs to DARDAR observations from February 2007 to 2010. Overshooting convection occurs so infrequently (Figure 8) compared to cirrus that imposing an upper limit on the RACP cirrus definition to exclude overshooting tops does not make a noticeable difference in the overall cirrus frequencies.

For the GSRMs and observations, the areas of frequent RACP cirrus (Figure 11) tend to correspond well to the locations of frequent cold point-overshooting convection (Figure 8), consistent with the observed collocation of cirrus with deep convection in past studies (e.g., Lee et al., 2009; Sassen et al., 2009; Virts & Houze, 2015). In the observations (Figure 11a), there are frequent RACP cirrus over both land and ocean regions, with the highest occurrence over the Pacific warm pool.

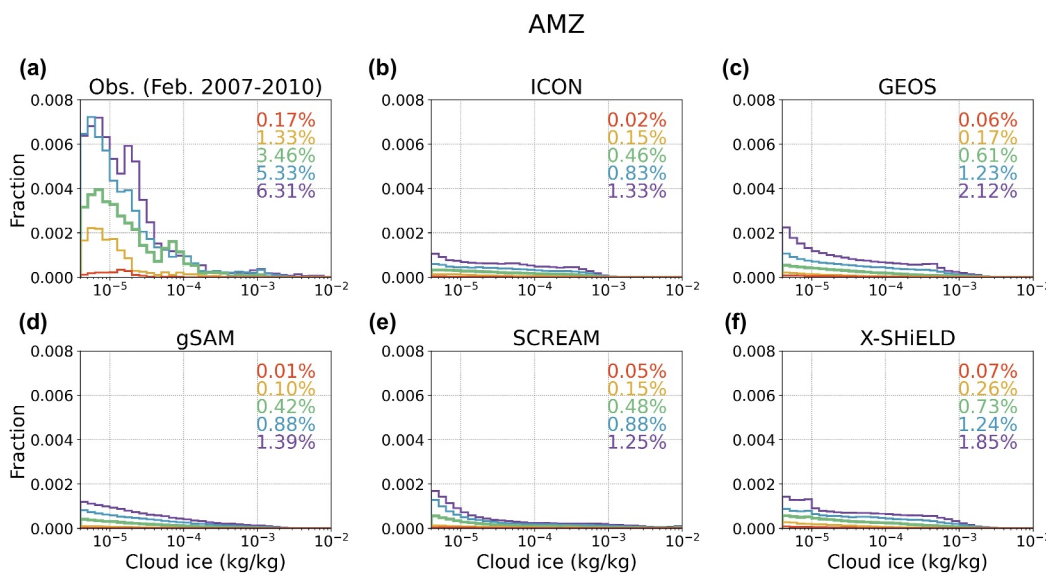

Figure 10. As in Figure 9, but for the AMZ. Note the different *y*-axis limits from Figure 9.

The GSRMs simulate similar amounts of RACP cirrus at z_{cp} (Figures 11b–11f), but vastly underestimate the amount that are detected by DARDAR (Figure 11a). If the radiative lofting of cirrus had a significant impact on the cold point, we would expect to see systematically lower and warmer cold points in the GSRMs since they do not produce enough cirrus that should be capable of radiative lofting. Based on Figure 3, this is clearly not the case. Therefore, there is little evidence that the radiative lofting of cirrus clouds near the cold point strongly affects the cold point temperature or height.

As explained in Section 6.1, we expect these results to be robust to the choice of minimum ice concentration for RACP cirrus. Adjusting the cloud ice threshold in either direction would not make the models simulate an appropriate amount of RACP cirrus compared to the observations.

7. Discussion

In this section, we relate the mean cold point (Figure 3), cold point-overshooting convection (Figure 8), and the lofting of RACP cirrus (Figure 11) to assess the relative importance of the two mechanisms in determining the cold point temperature and height during boreal winter. Comparing these three figures between models and between different regions in the same model reveals patterns in the relationships with the cold point temperature and height that are consistent in many of the GSRMs, despite differences in how they simulate cirrus and cold point overshoots.

Cold point overshoots are strongly related to the cold point height and temperature in the GSRMs and observations. This may indicate that the cold point-overshooting tops penetrate into the lower stratosphere and cool the surrounding air, leading to a colder and higher cold point. As noted by Gettelman et al. (2002), however, colder cold points may also allow convection to overshoot more often by destabilizing the upper troposphere. The relationship between cold point overshooting convection and the cold point itself may therefore work both ways; that is, overshoots cool and raise the cold point, and the colder cold points in turn make it easier for overshoots to occur.

Because the drastic difference in RACP cirrus frequency between the observations and GSRMs is not reflected in either the cold point height or temperature, there is little evidence that the radiative lofting of cirrus significantly affects the mean cold point. Any influence that the RACP cirrus have on the cold point is likely small or short-lived. Still, the collocation between areas of frequent cold point overshoots and frequent RACP cirrus suggests that the cold point overshoots help to form RACP cirrus, either directly through anvil detrainment or gravity wave temperature perturbations or indirectly by moistening the UTLS. Some of the RACP cirrus that loft above the cold point may evolve into the "other stratospheric cirrus" identified in Section 5.1. Still, the underestimation of cirrus near the cold point suggests that the GSRMs struggle to nucleate cirrus at such high altitudes, or maintain the cirrus that do form, with their current microphysics schemes.

A key limitation of this analysis is the lack of overlap between the time periods for the DARDAR observations used here (2007–2010) and the DYAMOND2 simulations (2020). This temporal mismatch introduces uncertainties into our model-observation comparisons. Still, the differences in the cirrus frequencies between the GSRMs and the DARDAR observations shown in Figures 9–11 exceed observed interannual differences in cirrus frequency, in particular the variability due to El Niño cycles (e.g., Virts & Wallace, 2010) where 2007–2010 and 2020 primarily differ (see Section 2.3). Therefore, the differences between observed cirrus frequency from 2007 to 2010 and 2020 likely would not explain the underestimation of cirrus near the cold point in GSRMs shown here. Similarly, we would not expect the interannual variations to change our conclusion that the radiative lofting of cirrus likely does not have a significant or lasting influence on the cold point.

The differences in cold point overshoots (Figure 8) and RACP cirrus (Figure 11) between GSRMs and observations are not sufficient to explain the differences in the mean cold points (Figure 3). Other processes aside from cold point-overshooting convection and radiative lofting must also play a primary role in setting the cold point. For example, the QBO or vertical disturbances from waves in the lower stratosphere may influence the cold point, but these processes occur on much longer timescales than the 40-day period of the DYAMOND2 runs and thus cannot be evaluated here. Shortwave and longwave radiation from processes or clouds other than RACP cirrus likely also play a significant role in setting the cold point tropopause. Still, the strong association between cold point overshoots and colder and higher cold points shown here suggests that cold point-overshooting convection is important for setting the cold point tropopause.

10.1029/2024EA003887

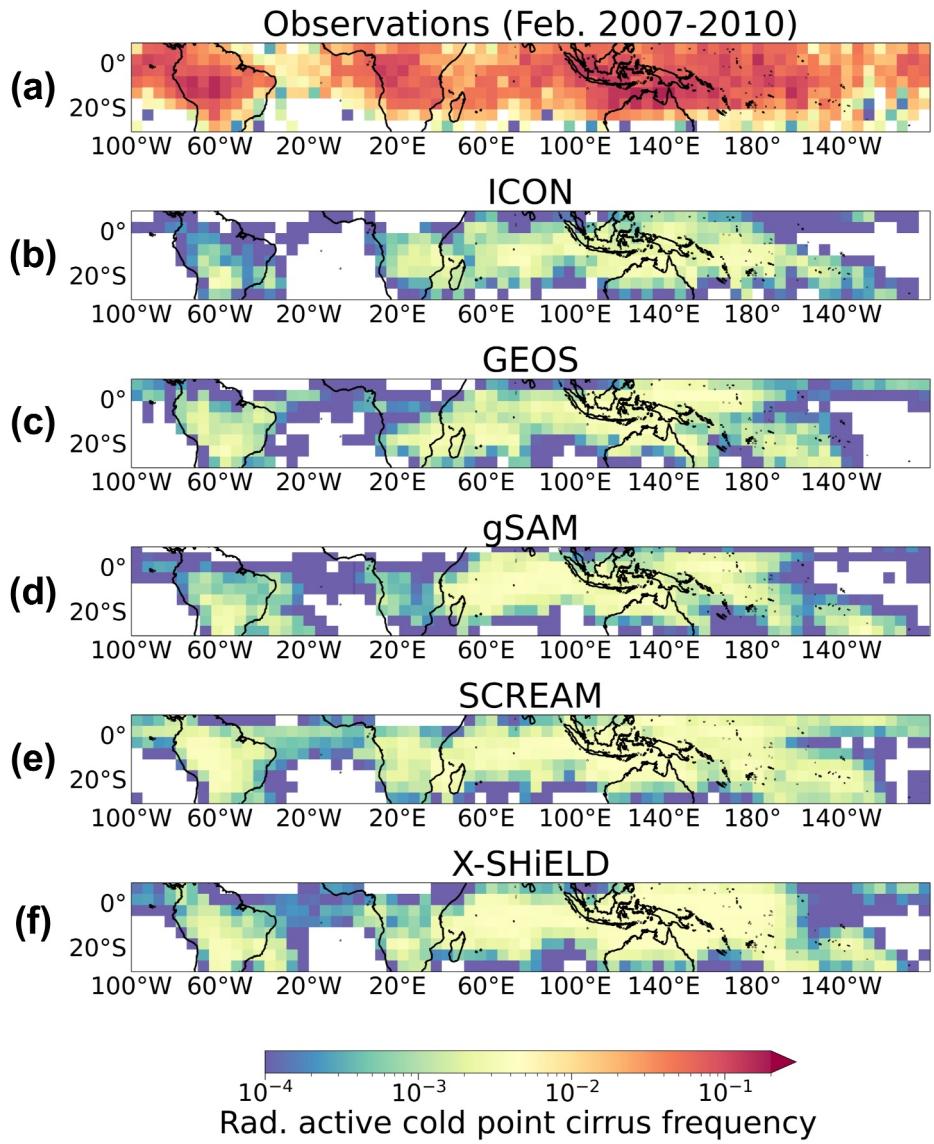

Figure 11. Frequency of radiatively active cold point cirrus in the 30-day period within 5° × 5° latitude-longitude boxes for (a) DARDAR observations and (b) ICON, (c) GEOS, (d) gSAM, (e) SCREAM, and (f) X-SHiELD GSRMs. All DARDAR retrievals for February 2007–2010 have been included.

8. Summary and Conclusions

In this study, we compare two possible mechanisms for altering the temperature and height of the tropical cold point tropopause: cold point-overshooting convection and the radiative lofting of cirrus clouds near the cold point. We use GSRMs and satellite observations during a 30-day period in boreal winter. We find that the models reproduce the observed geographic distribution in cold point-overshooting convection well. However, the GSRMs do not simulate enough cirrus compared to observations, including both thin cirrus above the cold point and RACP cirrus located at the cold point. Our results suggest that the cold point-overshooting convection has a non-negligible influence on the mean cold point temperature during boreal winter, acting to cool the cold point. The cold point overshoots likely help to form RACP cirrus, but cirrus lofting itself does not seem to significantly affect the mean cold point temperature or height. Although cold point-overshooting convection may influence the cold point tropopause, variations in cold point overshoots do not explain all variations in the cold point temperature or height shown here. Future studies quantifying the impact of cold point-overshooting convection on the

UTLS radiation budget compared to other processes are needed to fully untangle the relative importance of these mechanisms in determining the cold point temperature and height.

One major limitation of our study is the short time period of the simulations from the DYAMOND2 intercomparison. In models, the stratosphere can take up to 6 months to reach radiative equilibrium. Other stratospheric processes influencing the cold point also occur on much longer time scales, such as the QBO (Sweeney et al., 2023; Tegtmeier, Anstey, Davis, Ivanciu, et al., 2020) and Brewer-Dobson Circulation (Sweeney & Fu, 2024; Yu et al., 2022). Longer GSRM simulations like the recent 1- to 2-year X-SHiELD runs (Cheng et al., 2022; Harris et al., 2023; Merlis et al., 2024) are needed to untangle which processes are most important for determining the cold point temperature and height. Likewise, longer GSRM simulations would allow for this analysis to be repeated for seasons other than boreal winter, particularly boreal summer. Since the behavior of the cold point tropopause and the frequencies of overshooting convection and cirrus all vary seasonally (e.g., Nugent & Bretherton, 2023; W. Randel & Park, 2019; Sassen et al., 2009, respectively), an annual study would enable a more robust understanding of processes impacting the cold point tropopause in GSRMs. Additionally, future GSRM studies on the cold point tropopause would benefit from comparisons to a more robust set of observations, such as measurements of cirrus radiative heating rates or stratospheric water vapor from the Tropical Composition, Cloud, and Climate Coupling Experiment (TC4; Bucholtz et al., 2010; Selkirk et al., 2010; Toon et al., 2010) or ozonesonde-radiosonde measurements from the Southern Hemisphere Additional Ozonesondes project (SHADOZ; Thompson et al., 2004).

Nevertheless, we find that the DYAMOND2 GSRMs reproduce observed cold point overshoots and radiatively active cirrus well enough to study the cold point if compared to observations, providing an important starting point for better understanding the mechanisms controlling the cold point temperature and height in the real atmosphere. Further improvements in the model dynamics controlling vertical velocity (e.g., Atlas & Bretherton, 2023) and microphysics schemes, particularly how ice nucleation is represented (e.g., Seiki et al., 2022), are needed to correct the significant under-simulation of cirrus in the upper troposphere and lower stratosphere in GSRMs. Future studies using longer GSRM simulations would help further advance our understanding of the processes controlling the tropical cold point across seasons.

Data Availability Statement

DYAMOND2 model output is available from the German Climate Computing Center (DKRZ) through ESiWACE at https://easy.gems.dkrz.de/DYAMOND/. DARDAR data was provided by NASA and is available from the AERIS/ICARE Data and Services Center in Delanoë (2023). ERA5 reanalysis is available in Hersbach et al. (2017) and was downloaded using the CDS API from the Copernicus Climate Change Service. NCEP/CPC GPM_MERGIR data is available from NASA GES DISC in Janowiak et al. (2017). IGRA radiosonde data was obtained from the University of Wyoming through the Wyoming Weather Web at https://weather.uwyo.edu/upperair/sounding.html. Calculated Nino 3.4 Indices from the NOAA Extended Reconstructed SST V5 data set (Huang et al., 2017) and calculated 50 mb zonal-mean equatorial winds from NCEP/NCAR Reanalysis (Kalnay et al., 1996) were provided by the NOAA Physical Sciences Laboratory in Boulder, Colorado, USA and are available online at https://psl.noaa.gov/data/timeseries/month/Nino34_CPC/ and https://psl.noaa.gov/data/timeseries/month/DS/QBO50/, respectively. All code used for this analysis is publicly available on GitHub in Nugent (2025).

Acknowledgments
JN and PB were supported by the National Science Foundation through the Partnerships in International Research and Education program under Grant OISE-1743753. CB was supported by the Allen Institute for AI. Data management was provided by DKRZ and supported through the projects ESiWACE and ESiWACE2, which have received funding from the European Union's Horizon 2020 research and innovation program under grant agreements No 675191 and 823988. This work used resources of the DKRZ granted by its Scientific Steering Committee (WLA) under project IDs bk1040 and bb1153.

References

Ali, S., Mehta, S. K., Annamalai, V., Ananthavel, A., & Reddy, R. (2020). Qualitative observations of the cirrus clouds effect on the thermal structure of the tropical tropopause. *Journal of Atmospheric and Solar-Terrestrial Physics*, *211*, 105440. https://doi.org/10.1016/j.jastp.2020.105440

Atlas, R., & Bretherton, C. S. (2023). Aircraft observations of gravity wave activity and turbulence in the tropical tropopause layer: Prevalence, influence on cirrus clouds, and comparison with global storm-resolving models. *Atmospheric Chemistry and Physics*, *23*(7), 4009–4030. (Publisher: Copernicus GmbH). https://doi.org/10.5194/acp-23-4009-2023

Aumann, H. H., Behrangi, A., & Wang, Y. (2018). Increased frequency of extreme tropical deep convection: AIRS observations and climate model predictions. *Geophysical Research Letters*, *45*(24). https://doi.org/10.1029/2018GL079423

Avery, M. A., Davis, S. M., Rosenlof, K. H., Ye, H., & Dessler, A. E. (2017). Large anomalies in lower stratospheric water vapour and ice during the 2015-2016 El Niño. *Nature Geoscience*, *10*(6), 405–409. https://doi.org/10.1038/ngeo2961

Bechtold, P., Chaboureau, J.-P., Beljaars, A., Betts, A., Köhler, M., Miller, M., & Redelsperger, J.-L. (2004). The simulation of the diurnal cycle of convective precipitation over land in a global model. *Quarterly Journal of the Royal Meteorological Society*, *130*(604), 3119–3137. https://doi.org/10.1256/qj.03.103

Brewer, A. W. (1949). Evidence for a world circulation provided by the measurements of helium and water vapour distribution in the stratosphere. *Quarterly Journal of the Royal Meteorological Society*, *75*(326), 351–363. https://doi.org/10.1002/qj.49707532603

Bucholtz, A., Hlavka, D. L., McGill, M. J., Schmidt, K. S., Pilewskie, P., Davis, S. M., et al. (2010). Directly measured heating rates of a tropical subvisible cirrus cloud. *Journal of Geophysical Research*, *115*(D10). https://doi.org/10.1029/2009JD013128

Caldwell, P. M., Terai, C. R., Hillman, B., Keen, N. D., Bogenschutz, P., Lin, W., et al. (2021). Convection-permitting simulations with the E3SM global atmosphere model. *Journal of Advances in Modeling Earth Systems*, *13*(11). https://doi.org/10.1029/2021MS002544

Chae, J. H., Wu, D. L., Read, W. G., & Sherwood, S. C. (2011). The role of tropical deep convective clouds on temperature, water vapor, and dehydration in the tropical tropopause layer (TTL). *Atmospheric Chemistry and Physics*, *11*(8), 3811–3821. https://doi.org/10.5194/acp-11-3811-2011

Cheng, K.-Y., Harris, L., Bretherton, C., Merlis, T. M., Bolot, M., Zhou, L., et al. (2022). Impact of warmer sea surface temperature on the global pattern of intense convection: Insights from a global storm resolving model. *Geophysical Research Letters*, *49*(16), e2022GL099796. https://doi.org/10.1029/2022GL099796

Corti, T., Luo, B. P., Fu, Q., Vomel, H., & Peter, T. (2006). The impact of cirrus clouds on tropical troposphere-to-stratosphere transport. *Atmospheric Chemistry and Physics*, *9*.

Dauhut, T., & Hohenegger, C. (2022). The contribution of convection to the stratospheric water vapor: The first budget using a global storm-resolving model. *Journal of Geophysical Research: Atmospheres*, *127*(5). https://doi.org/10.1029/2021JD036295

Delanoë, J. (2023). DARDAR CLOUD—Heymfield's composite mass-size relationship. DARDAR-CLOUD v3.10 [Dataset]. *Aeris*. https://doi.org/10.25326/449

Dessler, A. E. (2002). The effect of deep, tropical convection on the tropical tropopause layer. *Journal of Geophysical Research*, *107*(D3), 4033. https://doi.org/10.1029/2001JD000511

Dessler, A. E., Schoeberl, M. R., Wang, T., Davis, S. M., & Rosenlof, K. H. (2013). Stratospheric water vapor feedback. *Proceedings of the National Academy of Sciences of the United States of America*, *110*(45), 18087–18091. https://doi.org/10.1073/pnas.1310344110

Dinh, T. P., Durran, D. R., & Ackerman, T. P. (2010). Maintenance of tropical tropopause layer cirrus. *Journal of Geophysical Research*, *115*(D2). https://doi.org/10.1029/2009JD012735

Duda, J. D., & Gallus, W. A. (2013). The impact of large-scale forcing on skill of simulated convective initiation and upscale evolution with convection-allowing grid spacings in the WRF. *Weather and Forecasting*, *28*(4), 994–1018. https://doi.org/10.1175/WAF-D-13-00005.1

Duras, J., Ziemen, F., & Klocke, D. (2021). The DYAMOND Winter data collection (Tech. Rep. No. EGU21-4687). In *Copernicus Meetings*. https://doi.org/10.5194/egusphere-egu21-4687

Fueglistaler, S., Dessler, A. E., Dunkerton, T. J., Folkins, I., Fu, Q., & Mote, P. W. (2009). Tropical tropopause layer. *Reviews of Geophysics*, *47*(1). https://doi.org/10.1029/2008RG000267

Gettelman, A., Salby, M. L., & Sassi, F. (2002). Distribution and influence of convection in the tropical tropopause region: Convection in the tropopause region. *Journal of Geophysical Research*, *107*(D10), ACL6–1–ACL6–12. https://doi.org/10.1029/2001JD001048

Harris, L., Zhou, L., Kaltenbaugh, A., Clark, S., Cheng, K.-Y., & Bretherton, C. (2023). A global survey of rotating convective updrafts in the GFDL X-SHiELD 2021 global storm resolving model. *Journal of Geophysical Research: Atmospheres*, *128*(10), e2022JD037823. https://doi.org/10.1029/2022JD037823

Harris, L., Zhou, L., Lin, S.-J., Chen, J.-H., Chen, X., Gao, K., et al. (2020). GFDL SHiELD: A unified system for weather-to-seasonal prediction. *Journal of Advances in Modeling Earth Systems*, *12*(10), e2020MS002223. https://doi.org/10.1029/2020MS002223

Hatsushika, H., & Yamazaki, K. (2001). Interannual variations of temperature and vertical motion at the tropical tropopause associated with ENSO. *Geophysical Research Letters*, *28*(15), 2891–2894. https://doi.org/10.1029/2001GL012977

Hersbach, H., Bell, B., Berrisford, P., Hirahara, S., Horányi, A., Muñoz-Sabater, J., et al. (2020). The ERA5 global reanalysis. *Quarterly Journal of the Royal Meteorological Society*, *146*(730), 1999–2049. https://doi.org/10.1002/qj.3803

Hersbach, H., Bell, B., Berrisford, P., Hirahara, S., Horányi, A., Muñoz-Sabater, J., et al. (2017). Complete ERA5 from 1940: Fifth generation of ECMWF atmospheric reanalyses of the global climate [Dataset]. *Copernicus Climate Change Service (C3S) Data Store (CDS)*. https://doi.org/10.24381/cds.143582cf

Highwood, E. J., & Hoskins, B. J. (1998). The tropical tropopause. *Quarterly Journal of the Royal Meteorological Society*, *124*(549), 1579–1604. https://doi.org/10.1002/qj.49712454911

Hoffmann, L., & Spang, R. (2022). An assessment of tropopause characteristics of the ERA5 and ERA-Interim meteorological reanalyses. *Atmospheric Chemistry and Physics*, *22*(6), 4019–4046. https://doi.org/10.5194/acp-22-4019-2022

Holton, J. R., & Gettelman, A. (2001). Horizontal transport and the dehydration of the stratosphere. *Geophysical Research Letters*, *28*(14), 2799–2802. https://doi.org/10.1029/2001GL013148

Huang, B., Thorne, P. W., Banzon, V. F., Boyer, T., Chepurin, G., Lawrimore, J. H., et al. (2017). NOAA extended reconstructed sea surface temperature (ERSST), Version 5 [Dataset; NOAA/CPC calculated Nino 3.4 SST Index]. *NOAA National Centers for Environmental Information*. https://doi.org/10.7289/V5T72FNM

Jain, A. R., Panwar, V., Johny, C. J., Mandal, T. K., Rao, V. R., Gautam, R., & Dhaka, S. K. (2011). Occurrence of extremely low cold point tropopause temperature during summer monsoon season: ARMEX campaign and CHAMP and COSMIC satellite observations. *Journal of Geophysical Research*, *116*(D3), D03102. https://doi.org/10.1029/2010JD014340

Janowiak, J., Joyce, B., & Xie, P. (2017). NCEP/CPC L3 half hourly 4km global (60°S–60°N) merged IR V1 [Dataset]. In A. Savtchenko (Ed.), *Greenbelt, MD, Goddard Earth Sciences Data and Information Services Center (GES DISC)*. https://doi.org/10.5067/P4HZB9N27EKU

Jensen, E. J., Toon, O. B., Selkirk, H. B., Spinhirne, J. D., & Schoeberl, M. R. (1996). On the formation and persistence of subvisible cirrus clouds near the tropical tropopause. *Journal of Geophysical Research*, *101*(D16), 21361–21375. https://doi.org/10.1029/95JD03575

Judt, F., Klocke, D., Rios-Berrios, R., Vanniere, B., Ziemen, F., Auger, L., et al. (2021). Tropical cyclones in global storm-resolving models. *Journal of the Meteorological Society of Japan Series II*, *99*(3), 579–602. https://doi.org/10.2151/jmsj.2021-029

Kalnay, E., Kanamitsu, M., Kistler, R., Collins, W., Deaven, D., Gandin, L., et al. (1996). The NCEP/NCAR reanalysis 40-year project. *Bulletin America Meteorology Social*, *77*(3), 437–471. https://doi.org/10.1175/1520-0477(1996)077<0437:tnyrp>2.0.co;2

Keeble, J., Hassler, B., Banerjee, A., Checa-Garcia, R., Chiodo, G., Davis, S., et al. (2021). Evaluating stratospheric ozone and water vapour changes in CMIP6 models from 1850 to 2100. *Atmospheric Chemistry and Physics*, *21*(6), 5015–5061. (Publisher: Copernicus GmbH). https://doi.org/10.5194/acp-21-5015-2021

Khairoutdinov, M. F., Blossey, P. N., & Bretherton, C. S. (2022). Global system for atmospheric modeling: Model description and preliminary results. *Journal of Advances in Modeling Earth Systems*, *14*(6), e2021MS002968. https://doi.org/10.1029/2021MS002968

Klocke, D., Brueck, M., Hohenegger, C., & Stevens, B. (2017). Rediscovery of the doldrums in storm-resolving simulations over the tropical Atlantic. *Nature Geoscience*, *10*(12), 891–896. https://doi.org/10.1038/s41561-017-0005-4

Krämer, M., Rolf, C., Luebke, A., Afchine, A., Spelten, N., Costa, A., et al. (2016). A microphysics guide to cirrus clouds—Part 1: Cirrus types. *Atmospheric Chemistry and Physics*, *16*(5), 3463–3483. https://doi.org/10.5194/acp-16-3463-2016

Kuang, Z., & Bretherton, C. S. (2004). Convective influence on the heat balance of the tropical tropopause layer: A cloud-resolving model study. *Journal of the Atmospheric Sciences*, *61*(23), 2919–2927. https://doi.org/10.1175/JAS-3306.1

Lee, J., Yang, P., Dessler, A. E., Gao, B.-C., & Platnick, S. (2009). Distribution and radiative forcing of tropical thin cirrus clouds. *Journal of the Atmospheric Sciences*, *66*(12), 3721–3731. https://doi.org/10.1175/2009JAS3183.1

Li, H., Wei, X., Min, M., Li, B., Nong, Z., & Chen, L. (2022). A dataset of overshooting cloud top from 12-year CloudSat/CALIOP joint observations. *Remote Sensing*, *14*(10), 2417. https://doi.org/10.3390/rs14102417

Lin, S.-J. (2004). A "Vertically Lagrangian" finite-volume dynamical core for global models. *Monthly Weather Review*, *132*(10), 2293–2307. https://doi.org/10.1175/1520-0493(2004)132⟨2293:AVLFDC⟩2.0.CO;2

Liou, K.-N. (2002). *An introduction to atmospheric radiation* (2nd ed.). Academic Press.

Liou, Y.-A., & Ravindra Babu, S. (2020). ENSO signatures observed in tropical tropopause layer parameters using long-term COSMIC RO data. *GPS Solutions*, *24*(4), 98. https://doi.org/10.1007/s10291-020-01009-7

Liu, C., & Zipser, E. J. (2005). Global distribution of convection penetrating the tropical tropopause. *Journal of Geophysical Research*, *110*(D23), D23104. https://doi.org/10.1029/2005JD006063

Merlis, T. M., Cheng, K.-Y., Guendelman, I., Harris, L., Bretherton, C. S., Bolot, M., et al. (2024). Climate sensitivity and relative humidity changes in global storm-resolving model simulations of climate change. *Science Advances*, *10*(26), eadn5217. https://doi.org/10.1126/sciadv.adn5217

Morrison, H., & Milbrandt, J. A. (2015). Parameterization of cloud microphysics based on the prediction of bulk ice particle properties. Part I: Scheme description and idealized tests. *Journal of the Atmospheric Sciences*, *72*(1), 287–311. https://doi.org/10.1175/JAS-D-14-0065.1

Nugent, J. M. (2025). DYAMOND-2 GSRM cold point-overshooting convection software [Software]. https://doi.org/10.5281/zenodo.15048415

Nugent, J. M., & Bretherton, C. S. (2023). Tropical convection overshoots the cold point tropopause nearly as often over warm oceans as over land. *Geophysical Research Letters*, *50*(21), e2023GL105083. https://doi.org/10.1029/2023GL105083

Nugent, J. M., Turbeville, S. M., Bretherton, C. S., Blossey, P. N., & Ackerman, T. P. (2022). Tropical cirrus in global storm-resolving models: 1. Role of deep convection. *Earth and Space Science*, *9*(2). https://doi.org/10.1029/2021EA001965

Pan, L. L., Honomichl, S. B., Bui, T. V., Thornberry, T., Rollins, A., Hintsa, E., & Jensen, E. J. (2018). Lapse rate or cold point: The tropical tropopause identified by in situ trace gas measurements. *Geophysical Research Letters*, *45*(19). https://doi.org/10.1029/2018GL079573

Pan, L. L., & Munchak, L. A. (2011). Relationship of cloud top to the tropopause and jet structure from CALIPSO data. *Journal of Geophysical Research*, *116*(D12), D12201. https://doi.org/10.1029/2010JD015462

Proud, S. R., & Bachmeier, S. (2021). Record-low cloud temperatures associated with a tropical deep convective event. *Geophysical Research Letters*, *48*(6). https://doi.org/10.1029/2020GL092261

Putman, W. M. (2021). Overcoming the challenges of increasing resolution and complexity in GEOS (Tech. Rep. No. EGU21-12782). In *Copernicus Meetings*. https://doi.org/10.5194/egusphere-egu21-12782

Putman, W. M., & Lin, S.-J. (2007). Finite-volume transport on various cubed-sphere grids. *Journal of Computational Physics*, *227*(1), 55–78. https://doi.org/10.1016/j.jcp.2007.07.022

Putman, W. M., & Suarez, M. (2011). Cloud-system resolving simulations with the NASA Goddard Earth Observing System global atmospheric model (GEOS-5). *Geophysical Research Letters*, *38*(16). https://doi.org/10.1029/2011GL048438

Randel, W., & Park, M. (2019). Diagnosing observed stratospheric water vapor relationships to the cold point tropical tropopause. *Journal of Geophysical Research: Atmospheres*, *124*(13), 7018–7033. https://doi.org/10.1029/2019JD030648

Randel, W. J., & Jensen, E. J. (2013). Physical processes in the tropical tropopause layer and their roles in a changing climate. *Nature Geoscience*, *6*(3), 169–176. https://doi.org/10.1038/ngeo1733

Randel, W. J., Seidel, D. J., & Pan, L. L. (2007). Observational characteristics of double tropopauses. *Journal of Geophysical Research*, *112*(D7). https://doi.org/10.1029/2006JD007904

Sassen, K., Wang, Z., & Liu, D. (2009). Cirrus clouds and deep convection in the tropics: Insights from CALIPSO and CloudSat. *Journal of Geophysical Research*, *114*(D4), D00H06. https://doi.org/10.1029/2009JD011916

Seidel, D. J., Ross, R. J., Angell, J. K., & Reid, G. C. (2001). Climatological characteristics of the tropical tropopause as revealed by radiosondes. *Journal of Geophysical Research*, *106*(D8), 7857–7878. https://doi.org/10.1029/2000JD900837

Seiki, T., Roh, W., & Satoh, M. (2022). Cloud microphysics in global cloud resolving models. *Atmosphere-Ocean*, *60*(3–4), 1–29. https://doi.org/10.1080/07055900.2022.2075310

Selkirk, H. B., Vömel, H., Valverde Canossa, J. M., Pfister, L., Diaz, J. A., Fernández, W., et al. (2010). Detailed structure of the tropical upper troposphere and lower stratosphere as revealed by balloon sonde observations of water vapor, ozone, temperature, and winds during the NASA TCSP and TC4 campaigns. *Journal of Geophysical Research*, *115*(D10). https://doi.org/10.1029/2009JD013209

Solomon, S., Rosenlof, K. H., Portmann, R. W., Daniel, J. S., Davis, S. M., Sanford, T. J., & Plattner, G.-K. (2010). Contributions of stratospheric water vapor to decadal changes in the rate of global warming. *Science*, *327*(5970), 1219–1223. https://doi.org/10.1126/science.1182488

Stevens, B., Satoh, M., Auger, L., Biercamp, J., Bretherton, C. S., Chen, X., et al. (2019). DYAMOND: The DYnamics of the atmospheric general circulation modeled on non-hydrostatic domains. *Progress in Earth and Planetary Science*, *6*(1), 61. https://doi.org/10.1186/s40645-019-0304-z

Suneeth, K. V., Das, S. S., & Das, S. K. (2017). Diurnal variability of the global tropical tropopause: Results inferred from COSMIC observations. *Climate Dynamics*, *49*(9–10), 3277–3292. https://doi.org/10.1007/s00382-016-3512-x

Sweeney, A., & Fu, Q. (2024). Interannual variability of zonal mean temperature, water vapor, and clouds in the tropical tropopause layer. *Journal of Geophysical Research: Atmospheres*, *129*(3), e2023JD039002. https://doi.org/10.1029/2023JD039002

Sweeney, A., Fu, Q., Pahlavan, H. A., & Haynes, P. (2023). Seasonality of the QBO impact on equatorial clouds. *Journal of Geophysical Research: Atmospheres*, *128*(7), e2022JD037737. https://doi.org/10.1029/2022JD037737

Takahashi, H., & Luo, Z. J. (2014). Characterizing tropical overshooting deep convection from joint analysis of CloudSat and geostationary satellite observations: Tropical deep convection by CLOUDSAT. *Journal of Geophysical Research: Atmospheres*, *119*(1), 112–121. https://doi.org/10.1002/2013JD020972

Tegtmeier, S., Anstey, J., Davis, S., Dragani, R., Harada, Y., Ivanciu, I., et al. (2020). Temperature and tropopause characteristics from reanalyses data in the tropical tropopause layer. *Atmospheric Chemistry and Physics*, *20*(2), 753–770. https://doi.org/10.5194/acp-20-753-2020

Tegtmeier, S., Anstey, J., Davis, S., Ivanciu, I., Jia, Y., McPhee, D., & Pilch Kedzierski, R. (2020). Zonal asymmetry of the QBO temperature signal in the tropical tropopause region. *Geophysical Research Letters*, *47*(24), e2020GL089533. https://doi.org/10.1029/2020GL089533

Thompson, A. M., Witte, J. C., Oltmans, S. J., & Schmidlin, F. J. (2004). SHADOZ—A tropical ozonesonde–radiosonde network for the atmospheric community. *Bulletin of the American Meteorological Society*, *85*(10), 1549–1564. https://doi.org/10.1175/BAMS-85-10-1549

Toon, O. B., Starr, D. O., Jensen, E. J., Newman, P. A., Platnick, S., Schoeberl, M. R., et al. (2010). Planning, implementation, and first results of the tropical composition, cloud and climate coupling experiment (TC4). *Journal of Geophysical Research*, *115*(D10). https://doi.org/10.1029/2009JD013073

Turbeville, S. M., Nugent, J. M., Ackerman, T. P., Bretherton, C. S., & Blossey, P. N. (2022). Tropical cirrus in global storm-resolving models: 2. Cirrus life cycle and top-of-atmosphere radiative fluxes. *Earth and Space Science*, *9*(2). https://doi.org/10.1029/2021EA001978

Virts, K. S., & Houze, R. A. (2015). Clouds and water vapor in the tropical tropopause transition layer over mesoscale convective systems. *Journal of the Atmospheric Sciences*, *72*(12), 4739–4753. https://doi.org/10.1175/JAS-D-15-0122.1

Virts, K. S., & Wallace, J. M. (2010). Annual, interannual, and intraseasonal variability of tropical tropopause transition layer cirrus. *Journal of the Atmospheric Sciences*, *67*(10), 3097–3112. https://doi.org/10.1175/2010JAS3413.1

Wu, X., Fu, Q., & Kodama, C. (2023). Response of tropical overshooting deep convection to global warming based on global cloud-resolving model simulations. *Geophysical Research Letters*, *50*(14), e2023GL104210. https://doi.org/10.1029/2023GL104210

Xian, T., & Fu, Y. (2015). Characteristics of tropopause-penetrating convection determined by TRMM and COSMIC GPS radio occultation measurements: Tropopause-penetrating convection. *Journal of Geophysical Research: Atmospheres*, *120*(14), 7006–7024. https://doi.org/10.1002/2014JD022633

Xie, F., Li, J., Tian, W., Li, Y., & Feng, J. (2015). Indo-pacific warm pool area expansion, modoki activity and tropical cold-point tropopause temperature variations. *Scientific Reports*, *4*(1), 4552. https://doi.org/10.1038/srep04552

Yu, W., Garcia, R., Yue, J., Russell, J., III., & Mlynczak, M. (2022). Variability of water vapor in the tropical middle atmosphere observed from satellites and interpreted using SD-WACCM simulations. *Journal of Geophysical Research: Atmospheres*, *127*(13), e2022JD036714. https://doi.org/10.1029/2022JD036714

Zängl, G., Reinert, D., Rípodas, P., & Baldauf, M. (2015). The ICON (ICOsahedral Non-hydrostatic) modelling framework of DWD and MPI-M: Description of the non-hydrostatic dynamical core. *Quarterly Journal of the Royal Meteorological Society*, *141*(687), 563–579. https://doi.org/10.1002/qj.2378

Zhou, X., & Holton, J. R. (2002). Intraseasonal variations of tropical cold-point tropopause temperatures. *Journal of Climate*, *15*(12), 1460–1473. https://doi.org/10.1175/1520-0442(2002)015⟨1460:IVOTCP⟩2.0.CO;2

Zhou, X.-L., Geller, M. A., & Zhang, M. (2001a). Cooling trend of the tropical cold point tropopause temperatures and its implications. *Journal of Geophysical Research*, *106*(D2), 1511–1522. https://doi.org/10.1029/2000JD900472

Zhou, X. L., Geller, M. A., & Zhang, M. H. (2001b). Tropical cold point tropopause characteristics derived from ECMWF reanalyses and soundings. *Journal of Climate*, *14*(8), 1823–1838. https://doi.org/10.1175/1520-0442(2001)014⟨1823:TCPTCD⟩2.0.CO;2

Zipser, E. J., Cecil, D. J., Liu, C., Nesbitt, S. W., & Yorty, D. P. (2006). Where are the most intense thunderstorms on earth? *Bulletin of the American Meteorological Society*, *87*(8), 1057–1072. https://doi.org/10.1175/BAMS-87-8-1057